

Article

Shoreline Delineation from Synthetic Aperture Radar (SAR) Imagery for High and Low Tidal States in Data-Deficient Niger Delta Region

Emmanuel Chigozie Dike ^{1,2,*}, Abiodun Kolawole Oyetunji ^{1,3} and Chiemela Victor Amaechi ^{4,5,6,*}

¹ Lancaster Environment Centre (LEC), Lancaster University, Lancaster LA1 4YQ, UK; abiodunoyetunji@gmail.com

² Department of Urban and Regional Planning, Rivers State University, Port Harcourt 500101, Nigeria

³ Department of Estate Management, University of Benin, Benin City 300287, Nigeria

⁴ School of Engineering, Lancaster University, Bailrigg, Lancaster LA1 4YR, UK

⁵ Standards Organisation of Nigeria (SON), 52 Lome Crescent, Wuse Zone 7, Abuja 900287, Nigeria

⁶ Institute of Energy Infrastructure, Universiti Tenaga Nasional (The National Energy University), Jalan IKRAM-UNITEN, Kajang 43000, Malaysia

* Correspondence: decfoundation@gmail.com (E.C.D.); chiemelavic@gmail.com (C.V.A.)

Abstract: Satellite image analysis is a potentially powerful tool for monitoring coastal shoreline positions. This study explores the use of multi-temporal, dual-polarised Sentinel-1 GRD synthetic aperture radar (SAR) imagery with a spatial resolution of 10 m for delineating shorelines. It was conducted in a data-deficient and complex environment (the Niger delta of Nigeria), in a developing country with a cloud-heavy climate. The study focuses on exploring and testing the capability of using multitemporal waterlines from SAR images to derive shoreline positions at high and low tidal states. From 54 Sentinel-1 images recorded in 2017, the study selected 12 images to represent both high and low tidal states. These were spread across the wet and dry seasons in order to account for seasonal differences. Shoreline positions were obtained by identifying the land–water boundary via segmentation using histogram-minimum thresholding, vectorizing and smoothing that boundary, and averaging its position over multiple waterlines. The land–water segmentation had an overall accuracy of 95–99%. It showed differences between wet and dry season shoreline positions in areas dominated by complex creek networks, but similarities along open coasts. The SAR-derived shorelines deviated from the reference lines by a maximum of 43 m (approximately four pixels), and often less than 10 m (one pixel) in most locations (open coast, estuarine, complex creek networks) at high and low tides, except low tide lines in areas with extensive inter-tidal flats at shorelines 70 m to 370 m from the reference lines. However, for applications such as coastal vulnerability assessment, the high tide shoreline is of greater importance. Thus, depending on the application of interest, problems with low tide shoreline delineation may be irrelevant. Despite limitations, notably the relatively small number of images available that were recorded at high or low tide, the method provides a simple, objective, and cost-effective approach to monitoring shorelines at high and low tide.

Keywords: shoreline delineation; synthetic aperture radar (SAR); backscatter; thresholding; vectorizing; positional accuracy; coastal data; Niger Delta



Citation: Dike, E.C.; Oyetunji, A.K.; Amaechi, C.V. Shoreline Delineation from Synthetic Aperture Radar (SAR) Imagery for High and Low Tidal States in Data-Deficient Niger Delta Region. *J. Mar. Sci. Eng.* **2023**, *11*, 1528. <https://doi.org/10.3390/jmse11081528>

Academic Editor: Charitha Pattiaratchi

Received: 17 June 2023

Revised: 23 July 2023

Accepted: 26 July 2023

Published: 31 July 2023



Copyright: © 2023 by the authors. Licensee MDPI, Basel, Switzerland. This article is an open access article distributed under the terms and conditions of the Creative Commons Attribution (CC BY) license (<https://creativecommons.org/licenses/by/4.0/>).

1. Introduction

Coastal shorelines are affected by a combination of natural processes and human-induced changes. The natural processes of erosion and accretion that transform their configuration are caused by both extreme weather events and more common wave, wind and tidal states acting over long timescales. Globally, there is an increasing need for monitoring the shoreline position in order to track climate change-induced sea-level rises (SLR). Various studies have shown that satellite image analysis is a potentially powerful tool

for monitoring coastal shoreline positions [1–4] as well as shoreline management strategies [5–8]. Shoreline position information is also crucial for coastal scientists and modellers, who need it to understand sediment transport and assess sediment budgets [9,10], predict the rates of coastal land loss or gain over time [11–14] and provide measures for assessing coastal vulnerability [7,8,15]. In a practical context, this information is used by coastal managers to inform day-to-day and long-term planning; thus, it requires substantial spatial and temporal coverage, as well as high accuracy. A range of remote sensing techniques can be applied for shoreline monitoring, captured from some video cameras (which can be based on relatively small spatial scales), to light detection and ranging (LiDAR) devices (medium spatial scale) and satellite imagery (large spatial scale). Freely available satellite imagery with high spatial and temporal resolution provides an important source of data for shoreline detection, particularly in developing countries where ground-based monitoring is not extensive. However, shoreline determination from such imagery has many challenges.

There are two steps to defining a shoreline; firstly, a suitable coastal indicator feature needs to be defined, and secondly, this needs to be used to detect the shoreline within the available data source [15]. In theory, the shoreline is defined as a spatially continuous line of contact between the land and a body of water [15]. This concept is simple, but in practice, shoreline delineation is complicated due to temporal variability across many timescales, ranging from quasi-instantaneous changes to super-annual scale changes caused by hydrodynamic phenomena such as waves and tides, and geomorphological changes due to erosion and accretion [16]. Furthermore, the precise identification of the shoreline position can be complicated by near-continuous across-shore gradients from shallow water to wet sand or mud to drier land surfaces, which can frequently occur over tens of metres. Boak and Turner [15] outline different shoreline indicators, which are grouped into three categories. The first category is based on visually recognisable coastal elements, which are physically seen (i.e., permanent dry/wet land). The second category is based on tidal datum-based shoreline indicators, which are determined by the intersection of a coastal profile with a specific vertical elevation. Often the mean water level (MWL), the mean high spring tidal level or the mean high neap tidal level are used. The final category is based on the application of image processing techniques which are used to delineate proxy shoreline features from coastal remote sensing imagery that are not visible to the human eye. Researchers have used several indicators in the third category as satellite technology has advanced and its ability to objectively delineate a range of shorelines in a robust and repeatable manner has evolved. A recent study by Paz-Delgado et al. [17] examined how synthetic aperture radar (SAR) and multi-spectral imagery (MSI) used publicly available satellite images in mapping, detecting, and capturing the coastline variations (both inter-annual and sub-annual) in three coastlines in England, namely gravel pocket-beach, soft cliff environment, and estuarine. However, it is important to note that any delineated shoreline indicator does not necessarily represent the “actual” shoreline, however that may be defined [18]. Zheng et al. [19] used SAR-imagery to present correction criteria in investigating coastline areas using a waterline extraction approach and obtained an automatic method for the coastline extraction.

Historically, the first optical satellite launch in 1972 advanced the course of digital image processing, of the geographic information system (GIS) and of remote sensing. This first land observation satellite, called Landsat-1, had a revolutionary multispectral scanner (MSS), which delivered digital time sequence array as a way of transferring data [20]. Since the launch of that first optical satellite in 1972, satellite images have been used to delineate shoreline positions, such as the use of tidal lines and water lines. According to Niedermeier et al. [21], the waterline is defined as the instantaneous land–water boundary at the time of the imaging process to differentiate them from the coastlines, while shorelines are defined both in temporal and spatial senses and must take into account waterline variability on the time scale of the image processing [15]. As the rest of this study is focused on shoreline delineation, which will be used, more background on this study is important. Researchers have used a variety of moderate and high-resolution optical satellite sensor

imagery for shoreline delineation. These multispectral imageries have contributed to shoreline delineation globally, but their applicability has been limited due to factors such as cloud cover, cloud shadow, haze from rainfall, snowy climes, ice formations and sun glint. A number of researchers have developed index- and threshold-based techniques for delineating the shoreline position and change over time from optical imagery including the Normalised Difference Vegetation Index (NDVI) [22], Normalised Difference Water Index (NDWI) [23,24], Modified Normalised Water Index (MDWI) [25], Tasselled Cap Wetness index (TCW) [26,27], and Automated Water Extraction Index (AWEI) [19,28]. Vos et al. [29] recently introduced a Google Earth Engine-enabled python toolkit for delineating coastlines from optical satellite-based imagery in Australia. However, such indices are less effective in areas where cloud cover dominates for much of the year, or in complex intertidal environments, where the position of the shoreline can change rapidly depending on the state of the tide or storm surges. In general, there is no widely accepted technique for delineating shorelines from optical imagery since each technique has its own limitations regardless of the imagery and the nature of the environment in which the technique is applied [30].

In contrast to optical image acquisition systems, synthetic aperture radar (SAR) satellite systems have all-weather day–night imaging capabilities. Since their introduction in 1978, several methods have been developed to delineate shorelines from data generated using different SAR satellite sensors. A number of researchers have used edge detection techniques to determine shoreline position. For example, Lee and Jurkevich [31] developed an edge detection algorithm for shoreline delineation based on an edge tracing algorithm. This showed reasonable accuracy when visually assessed but required further refinement in order to achieve the required accuracy for geospatial applications. Mason and Davenport [32] developed a semi-automatic technique to delineate shoreline position from ERS-1 SAR imagery, using the imagery to develop a digital elevation model (DEM) of the intertidal area, which was subsequently used in a hydrodynamic model. Niedermeier et al. [9] employed wavelet-based edge detection techniques and active contour algorithms to derive shoreline positions from SAR imagery. The accuracy of land–water segmentation using wavelet-based edge detection was compared to the outputs of a block-tracing algorithm, with the results indicating that 85% of the edge points were within two pixels of the derived shoreline. Spinosa et al. [33] adopted automated edge detection techniques to delineate shoreline position from Sentinel-1 SAR imagery. The satellite-derived shoreline was validated against an in situ video-derived shoreline whose spatial resolution varied from decimetres to approximately 13 m based on the distance of the camera footprint along the nearshore. The result revealed a positional accuracy of about 10 m and a root mean square difference (RMSD) of 21.48 m. Wang and Liu [34] adopted a robust ridge tracing method to delineate shoreline position from RADARSAT-2 and Sentinel-1 SAR images. The method proved effective when compared to the ridge tracing technique with an in-situ video monitoring system. The video imagery was then used to evaluate the accuracy of the two delineated SAR images using pixel radii percentages. The results indicated that the level of agreement between the derived shorelines from optical images and SAR images varied at different locations. Generally, most of the delineation approaches are simple and robust, though the use of a single SAR image polarisation gave discontinuous outcomes, which are inconsistent with reality, as shoreline are continuous features.

A range of analysis have been conducted in various studies using SAR imagery data obtained from Sentinel-1 satellite and good solutions to various environmental and marine concerns have been found (see [35–38]). Launched in 2014 and 2016, the Sentinel-1 SAR C-band imaging twin satellites (1A and 1B) provide all weather, day–night imagery for the coastal zone [39,40]. The SAR C-band instruments support operation in single-polarisation (HH or VV) or dual-polarisation (HH + HV or VV + VH) modes. Here, in the present study, in line with many previous studies, the focus is on the vertical-transmit polarisation options (VV and VH). Studies have shown that VV polarisation is more sensitive to incident wave angles and wind speeds than VH polarisation ([41,42]) due

to longer underlying waves which modify the Bragg scattering (Bragg waves) [42,43]. Similarly, other studies have shown that SAR backscatter depends on surface roughness and dielectric properties [44,45]. Mouche and Chapron [42] applied empirical model-based techniques to characterise the SAR backscatter as a function of local characteristics of soil moisture, while Altese et al. [44] utilised a theoretical model for a sensitivity assessment of soil moisture using the surface scattering model in an earlier study that combined the field data with SAR data. Consequently, the accuracy of a shoreline delineated from SAR imagery depends on external factors (i.e., wind, weather, wave, and tide conditions), and coastal sand moisture at the time of image acquisition. Using single-polarisation SAR images to delineate shoreline under different tidal conditions is challenging due to the mixed backscattering response resulting from variation of dry and wet sands and mudflats, which can lead to problems of misclassification.

There have been several studies of the extraction of shorelines from SAR satellite imagery, and more specifically the use of dual polarimetric systems to this end [46–48]. Ding et al. [49] explored this issue using Cosmo SkyMed data in a region of inter-tidal flats and found that both single- and dual-polarisation data identified waterlines ‘satisfactorily’, but that their accuracy decreased as the flats got wetter. Unsupervised classification of land and sea (and thus delineation of their boundary) was successful using the single-polarisation data when the land–sea contrast was high, but not when it was low or in complex areas. The same approach applied to dual polarisation data worked well under all these conditions. Others have focused on the application of alternative segmentation techniques to polarimetric SAR data, for example, fuzzy clustering [50] or K-means based methods [51]. More recently, Pelich et al. [52] put forward an automatic, unsupervised technique for deriving the mean shoreline position from a stack of Sentinel-1 dual-polarisation SAR images collected over a year and demonstrated that this was an effective way of reducing speckle whilst retaining high spatial resolution, as well as averaging over temporal variations at time scales of up to a year. They reported an agreement of 80–90% between their derived shorelines and Open Street Map (OSM) coastlines, and good agreement on a qualitative level with coastlines in optical Sentinel-2 imagery.

Thus, this present study extends the work of Pelich et al. [52], which delivered annual mean shoreline positions, and an earlier study by Dike et al. [53], which considered inter-tidal environments in shoreline delineation. Additionally, it later metamorphosed into the recently recorded SAR imagery in data-poor regions for reference lines using SAR-derived shorelines based on an accuracy approach [54]. This accuracy approach is supported by another study by Tajima et al. [55] that used a newly developed knowledge based on applying satellite SAR imagery using an artificial neural network (ANN) approach for shoreline detection, which found that most of the SAR images had classification accuracies of more than 95%. In comparison to this study, we found that most of the SAR images in the present study had overall accuracies of more than 95–99%. Thus, the aim of the study reported here is to explore and test the capability of using a stack of multiple SAR images to derive shoreline positions at high and low tidal states. This present study has the potential to provide greater insights into both the hydrodynamic and geomorphological aspects of coastal change and enable processes such as inter-tidal zone monitoring and management to be carried out more effectively. It will also test the relative capabilities of SAR imagery to distinguish between water and relatively dry land (at high tide) and water and recently wetted inter-tidal land surfaces (at low tide), and between these two states during wet and dry seasons, thus providing a more nuanced test of the applicability of this approach. Two important aspects of the study are that it is carried out in a region where (i) ground-based data are very sparse, and (ii) there is a mix of open coastlines with relatively simple geometry and complex regions of dendritic networks of inter-tidal channels. Therefore, the objectives of this study are as follows: (a) to develop a robust and repeatable segmentation technique to delineate waterline from multiple SAR images recorded around user-defined tidal states (high and low water in the present study); (b) to assess the accuracy of the derived shoreline at each tidal state against independent ref-

erence data; (c) to find and explain differences in the accuracy of this approach between high-water and low-water conditions during both the wet and dry seasons; and (d) to infer the implications of our findings for the application of this approach to aspects of coastal management. This paper is structured as follows: Section 1 introduces the paper, while Section 2 presents materials and methods. Section 3 presents the results of analysis, while Section 4 presents the discussion, and Section 5 presents the conclusions drawn.

2. Materials and Methods

2.1. Study Site

To develop the technique, imagery from the Niger Delta region was used. The Niger Delta is one of the most extensive wetlands in the world and contains an abundance of water bodies including estuaries, creeks, lakes, and streams. It is severely threatened by sea-level rise: projections estimate that over 250 km² of land in the coastal zone of the Niger Delta would be submerged if, as predicted, there is a 1 m rise in sea level by 2100 [56,57]. Due to the sensitive nature of the region in terms of capital investment, human and natural resources, it is estimated that the region will lose between USD 8.05 billion and USD 17.5 billion based on average sea level rises of 0.2 m and 1.0 m, respectively, by 2025 [57]. Accurate and up-to-date measurements of the shoreline are vital to support the assessment of coastal vulnerability and the development of mitigation strategies. Climatic conditions in this region make the acquisition of cloud-free optical imagery challenging, hence the attractiveness of imagery from all-weather SAR systems. While the Niger Delta region has a lot of oil and gas activities [58–60], there are various issues that require environmental monitoring in the area, such as oil spills [61–63] and sea level rise [2,64,65]. There are ranging levels of vulnerabilities to the Niger Delta coastline [2,53,54,65,66], which may be attributed to the fact that the Niger Delta coastline is low-lying, as reported by the IPCC [67]. However, there is no systematic sea level monitoring programme along the Niger Delta coastline; thus, comparisons with ground-based measurements to assess the accuracy of results derived from remotely sensed data are not possible. This constitutes an important aspect of the challenge addressed in this study. The study area is located along a 560 km section of coastline at the eastern distributary of the river Niger, which is the ninth longest river in the world and second longest in Africa (see Figure 1). In addition to the Niger River, many other rivers deposit sediments into the Gulf of Guinea in the eastern portion of the delta around the cities of New Calabar, Bonny, Imo and Qua Ibo. The region has a typically wet season (March to October) and dry season (December to February) with an annual rainfall of approximately 1900–3500 mm. During the wet season, tropical southwest winds from the Atlantic Ocean generate abundant rainfall, making the study area among the wettest regions on Earth [68]. The annual temperature of the area varies from 20 °C to 35 °C with high cloud cover and relative humidity ranging from 70 to 80%. The terrain of the region is low-lying, varying from 0 to 45 m above sea level [64] with a mean tidal range that increases eastwards from Bonny estuary (1.9 m) to Ibo river (3.0 m). Together, these factors make shoreline delineation especially challenging.

2.2. Data Selection

Multi-temporal Sentinel-1 Level 1 SAR C-band ground range detected (GRD) data were acquired from the European Space Agency (ESA) Copernicus Open Access Hub (<https://scihub.copernicus.eu/> last accessed on 12 July 2023). The technical information on the data repository and the Sentinel-1 SAR satellite are openly available online [39,40]. Interferogram Wide (IW) dual-polarisation (VV and VH) sensor images were downloaded for 100 km × 100 km tile scenes in UTM/WGS84 projection at 10 m spatial resolution. The year 2017 was chosen, arbitrarily, as the period on which the study focused, matching the length of the single year used by Pelich et al. [52] in their study of the overall average shoreline position, as described above. A total of 54 Sentinel-1 images were available for this year. The timing of these images was compared with tidal data measured at the city of Bonny (see Figure 1 for location), as shown in Figure 2. To delineate the shoreline at

low tide, the six images recorded when the tidal height at Bonny was below 1 m were used. A matching number of images (6) recorded when tidal height was above 2 m were selected from the total of 14 recorded at that tidal state. This selection for the high tide state was made arbitrarily in order to correspond to the available low tide data, which is less than 1 m (see Figure 2). The images from both the wet and dry seasons (roughly March to October and November to February, respectively) were used to allow the assessment of the variation in the ability of the method used to delineate the shorelines between them.

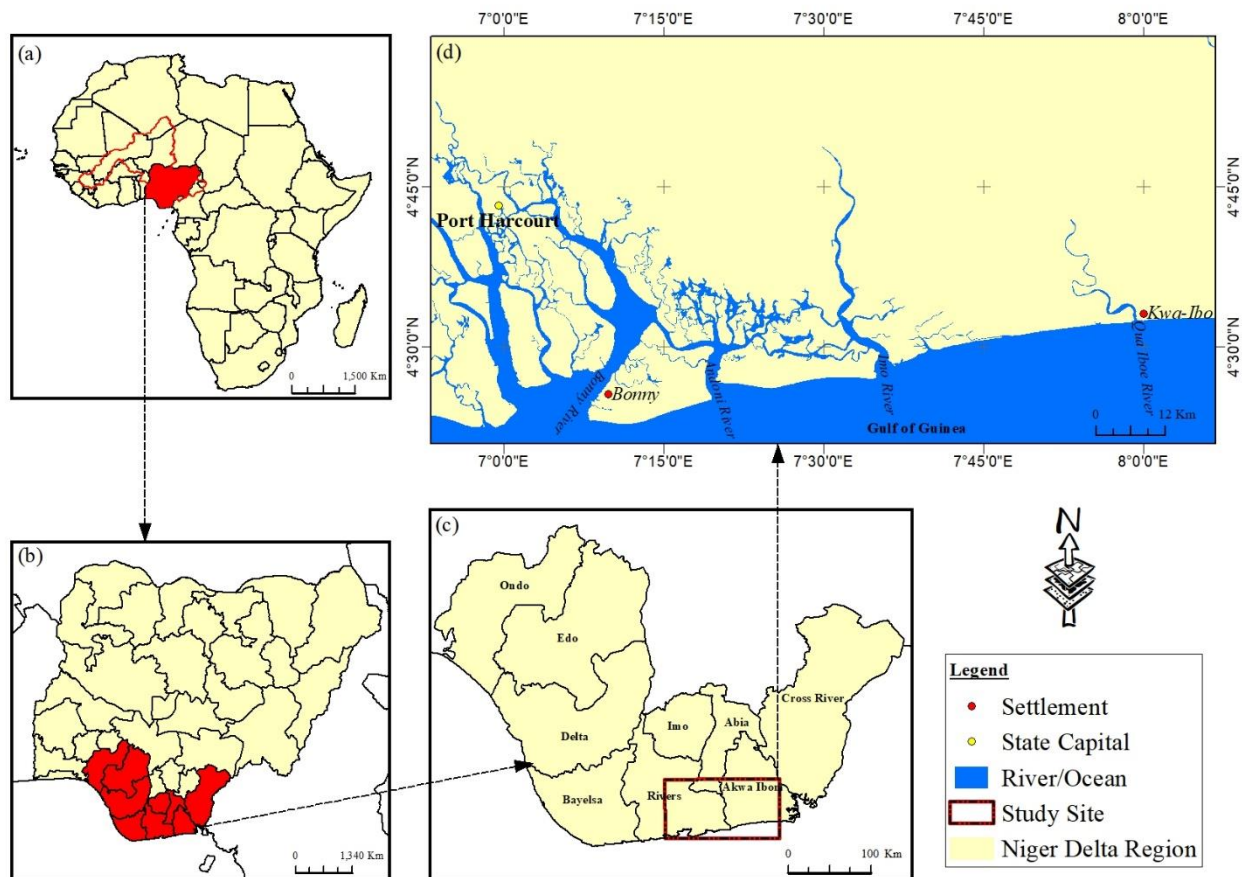


Figure 1. Maps showing (a) the African continent, (b) Nigeria, (c) the Niger Delta Region, and (d) the study area including the location of major settlements and river.

To assess the accuracy of the shorelines derived from the Sentinel-1 SAR images, multispectral optical Sentinel-2 imagery acquired on 25 January 2018 and 31 December 2017 at tidal heights of 2.1 m and 0.8 m, respectively, was utilised. It is worth noting that both images were captured during the dry season, when, presumably, coastal cloud cover is less of an issue. The Sentinel-2 multispectral instrument (MSI) has 13 spectral bands with spatial resolutions of 10, 20, 60 m. This study used the 10 m multispectral data, which are equivalent to the spatial resolution of the SAR data.

2.3. Data Collection and Processing

The technology under study is the adoption of SAR imagery and the procedure applied for the tidal data obtained from the Nigerian Naval Office in Bonny, Nigeria. The methodology adopted for deriving shoreline for high and low tides is summarised in Figure 3. Prior to shoreline delineation, the SAR images were pre-processed using the standard generic workflow for Sentinel images in the ESA Sentinel Application Platform (SNAP). To enable batch processing of the bulk images, a command graph-based procedure was adopted. Six standard correction procedures were applied to optimally reduce error dissemination in the resulting images, including precise orbit, radiometric calibration, and

range Doppler terrain correction. Other geographical data can also be obtained from public domain sites, while the vectorization of the waterline is achievable via standard tools available in most GIS software packages.

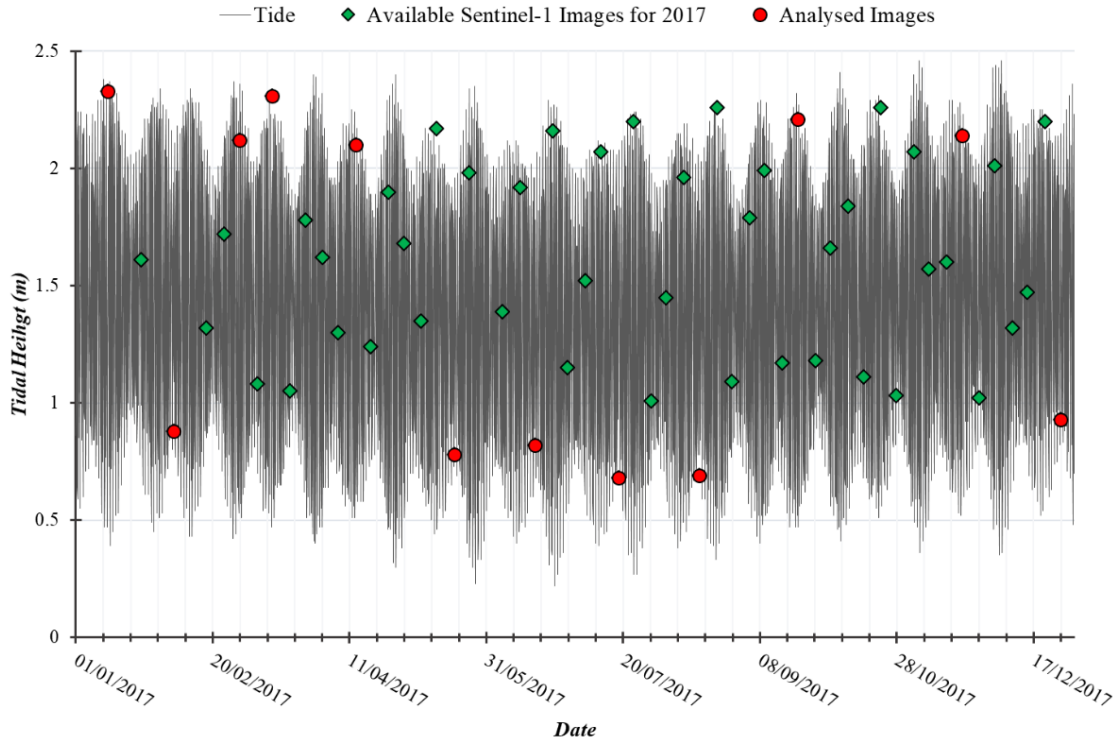


Figure 2. Tide height at Bonny Town for January 2017 to December 2017 showing Sentinel-1 images used in this study, marked in red (source: Nigerian Navy office, Bonny).

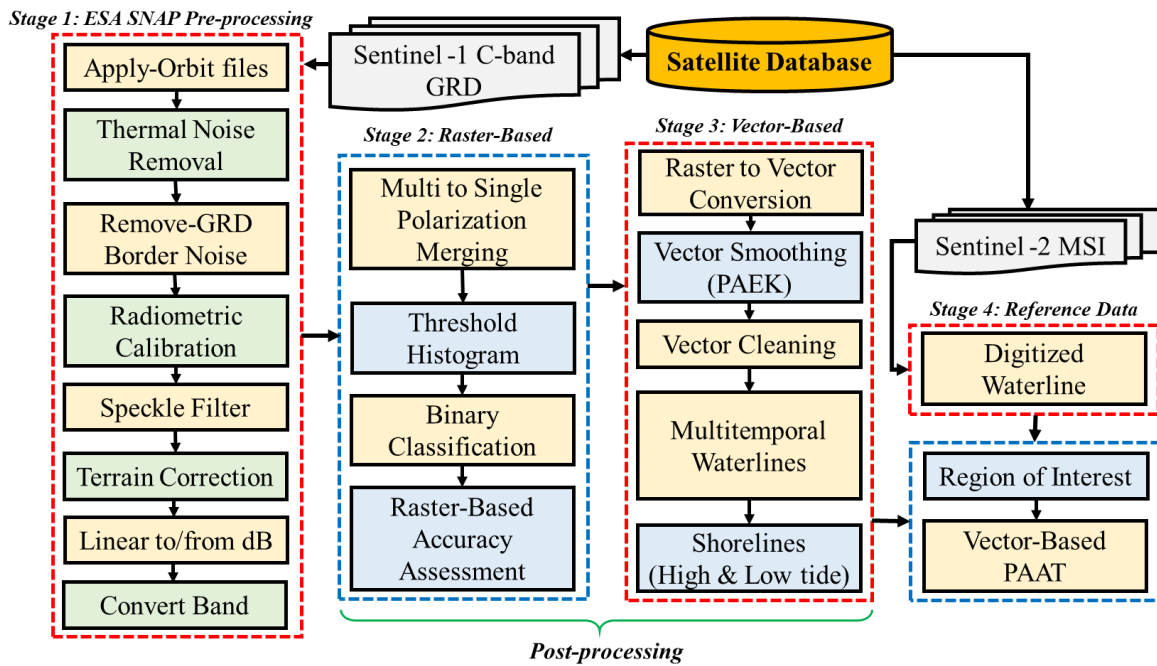


Figure 3. Flow diagram for the four stages of analysis image pre-processing, image classification and accuracy assessment, raster to vector conversion, and shoreline derivation at various tidal states.

2.4. Dual Polarisation Image Formation

The VV and VH polarisation data were combined and averaged into a single backscattered image. This is because wind and wave conditions are known to significantly impact the backscatter of the ocean surface, which affects SAR data, especially in VV polarisation, and thus affects shoreline delineation (e.g., [49,52]). The mean of the VV- and VH-polarised data was adopted, yielding lower backscatter intensity values for waterbodies and higher backscatter intensity values for dry sand and mudflat features (Figure 4). This makes it easier to distinguish land from water, particularly along sections of open coastline where the backscatter values in the VV and VH images showed considerable variation in the swash zone, which would have made shoreline delineation problematic if they had been used alone.

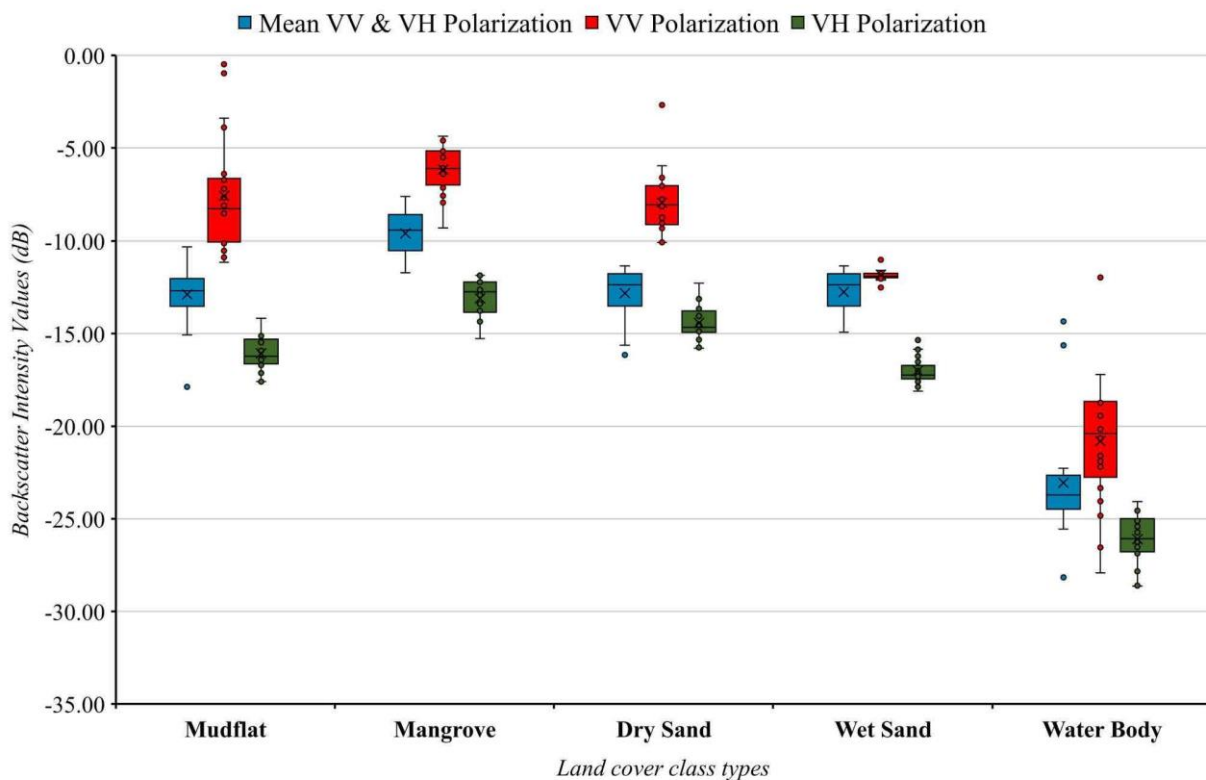


Figure 4. Backscatter pixel intensity of major land cover type.

In order to quantify the variation in the land cover types, the backscatter intensity values between the mean VV and VH, and VV and VH polarisation indicate variation in the reclassified land cover types (Table 1 and Figure 5). The mean VV and VH polarisation has proven to be effective for the delineation of land and water bodies. This is because based on the backscatter intensity values for the land cover, the minimum observation value for VV polarisation on the land is -12.0 , while the maximum observation value for the water body is -12.5 . Additionally, the VH polarisation demonstrates quite different backscatter intensity values with a minimum observation intensity value on the land of -18.1 and a maximum observation intensity value on the water body of -24.1 . Nevertheless, there are outlier backscatter intensity values observed in mean VV and VH polarisations for the land cover types as shown in Figures 4 and 5. In order to reduce this outlier problem, relative mean values of the two-land cover were used, which were applied to the threshold approach to classify the images.

Table 1. Overall polarisation backscatter intensity value for each land cover.

Reclassified Land Cover	Metric	Mean VV and VH	VV	VH
Land	Minimum	−17.9	−12.5	−18.1
	Maximum	−7.6	−0.5	−11.9
	Mean	−11.9	−8.4	−15.1
	Standard Deviation	1.9	2.8	1.8
Water Body	Minimum	−28.2	−27.9	−28.6
	Maximum	−14.3	−12.0	−24.1
	Mean	−23.0	−20.8	−26.1
	Standard Deviation	3.2	3.6	1.4

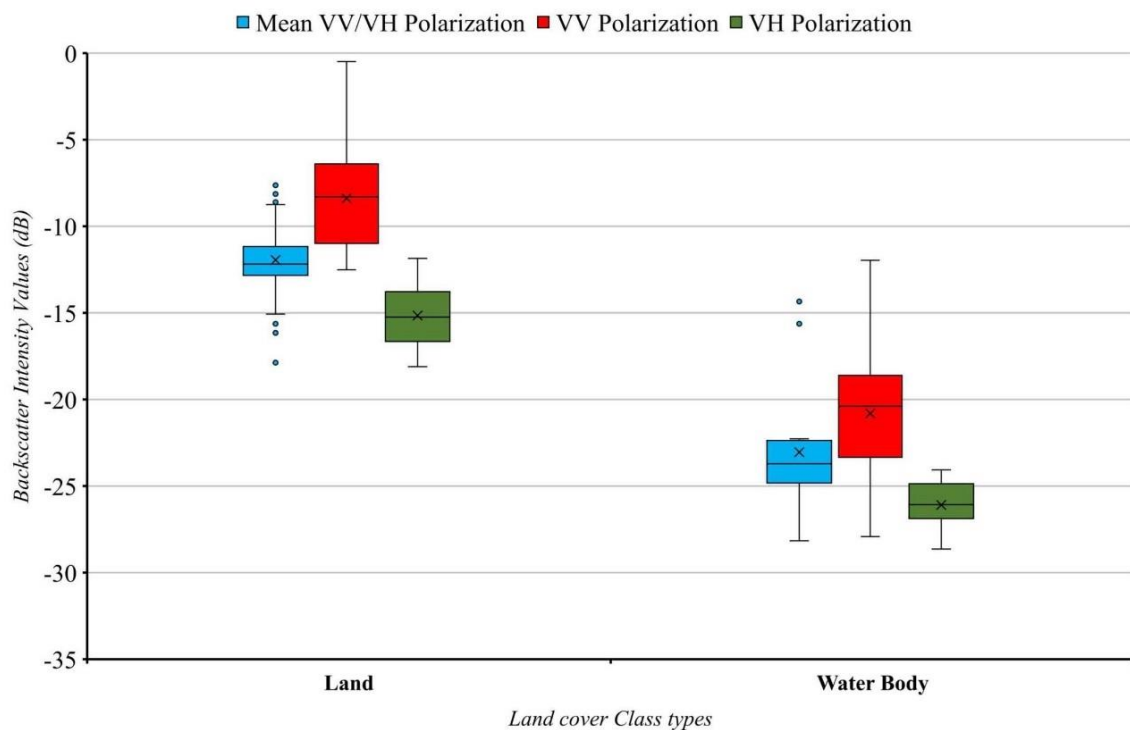


Figure 5. Backscatter intensity of reclassified land and water body.

2.5. Threshold-Based Segmentation

The averaged VV and VH backscatter images that cover both land and water surfaces have a bimodal frequency distribution of pixel intensities. A simple threshold approach was therefore used to differentiate between land and water in them. In theory, the backscatter value between the two peaks in the bimodal frequency distribution with the lowest frequency (pixel count) should be adopted as the threshold. However, due to the complexity of the images, which was confounded by noise in some cases, it was challenging to establish a single threshold that could be applied to all images. Therefore, this study utilised the backscatter value with the minimum intensity frequency between the peaks of multiple histograms. For example, in Figure 6, the averaged backscatter values from images recorded at multiple tidal states range from −33 dB (water) to +4 dB (land). A threshold value of −16.5 dB was adopted to the segment between water and land for all these images, which is the minima across the multiple histograms (see Figures 6 and 7).

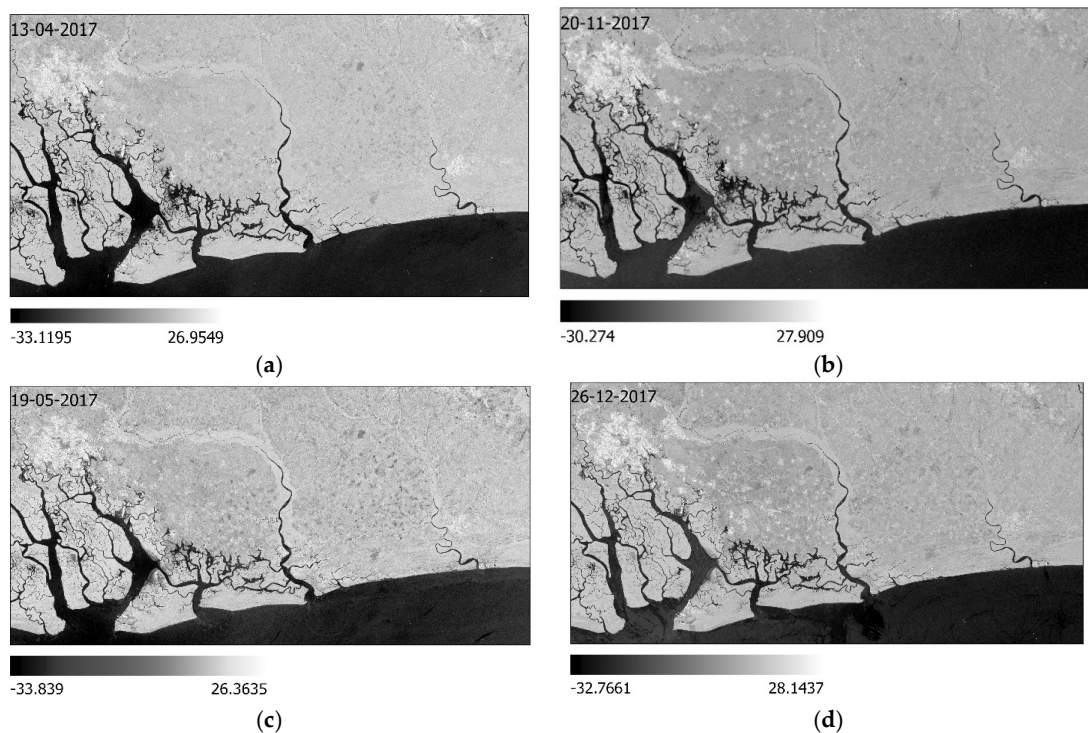


Figure 6. The (four) Sentinel-1 images, showing the images retrieved on (a) 13 April 2017, (b) 20 November 2017, (c) 19 May 2017, and (d) 26 December 2017.

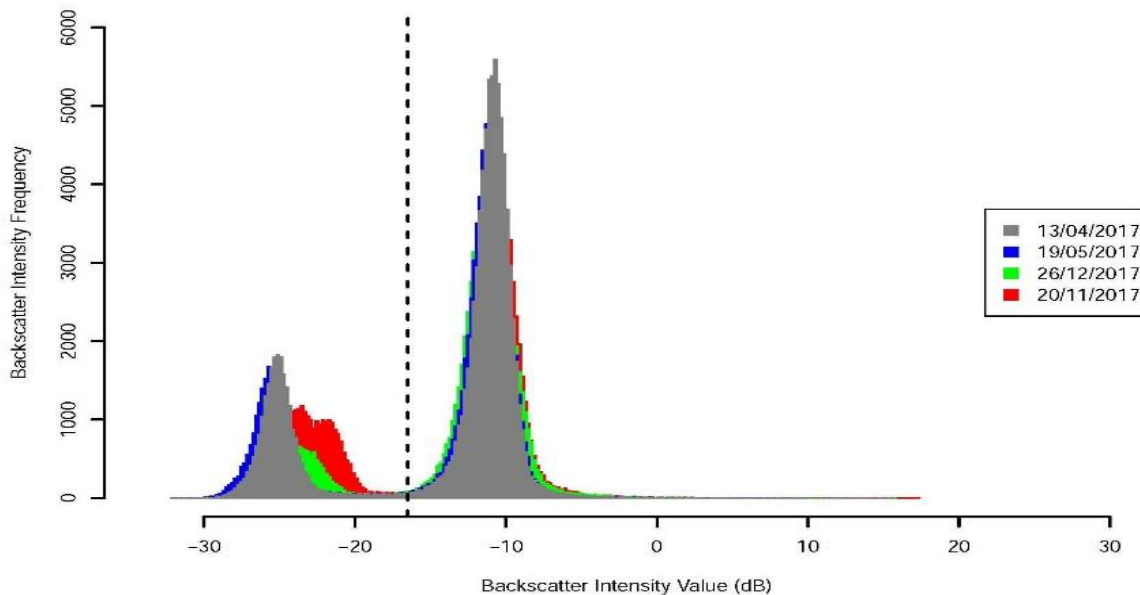


Figure 7. Histogram of backscatter for (four) Sentinel-1 images in Figure 6 above. The dashed black line represents the optimum threshold for binary classification into land and water classes.

2.6. Raster-Based Accuracy cum Confusion Matrices Assessment

The accuracy of the land–water classification of the Sentinel-1 SAR imagery was assessed against high-resolution Google Earth imagery captured on 21 December 2018 under low-tide conditions using confusion matrices, a widely used accuracy assessment technique [51,69]. An equalised stratified random sampling procedure was used in which reference points were captured from locations distributed evenly across the areas classified as land and water. The sample reference point data were then compared to equivalent data

from the SAR-based raster images to measure the levels of overall agreement. From these, a confusion matrix was created, from which producer's and user's accuracy could be calculated. An additional measure of accuracy, the kappa coefficient, was also calculated [24,28].

2.7. Raster-Featured cum Vector-Based Analysis

The ArcGIS raster-to-feature tool was used to convert the binary land–water images derived from the segmentation explained above into polygon features. The polygon features were converted to polylines which were then smoothed to improve their cartographic quality. This improvement was achieved using a polynomial approximation with exponential kernel (PAEK) algorithm which calculated a smooth line passing through the input vertices of the polylines with a smoothing tolerance of 40 m [70,71]. Lower levels of smoothing tolerance resulted in unacceptably jagged lines. Finally, a model-builder geoprocessing (i.e., conversion of multitemporal waterlines polylines into polygon, generalization (dissolve) from data management, topographic production (polygon to centreline) tool) approach was used to convert the multi-temporal vectorized waterlines into shorelines for high and low tide.

2.8. Positional Accuracy cum Vector-Based Assessment

In order to evaluate the positional accuracy of the derived MWLs, independent waterline datasets covering high and low tidal states were acquired by manually digitising Sentinel-2 MSI images. The vectorised MWLs derived from the Sentinel-1 SAR imagery were then assessed for positional accuracy against the Sentinel-2 image (reference data) using the ArcGIS 10.4 Positional Accuracy Assessment Tool (PAAT). PAAT is a point-based standard methodology (PBSM) which uses a series of measures to characterise the positional difference between two sets of geospatial data. It computes the random and systematic errors between a reference dataset and a target dataset, expressing differences through three metrics: mean residual, root mean square error (RMSE), and standard deviation [72–74]. Likewise, the degree of uncertainty is calculated using two metrics: absolute circular error (ACE) and relative circular error (RCE) at a 90% confidence level. The standards were developed in 1947 by the United States' National Standard for Spatial Data Accuracy (NSSDA), which was published in 1998 by the US Federal Geographic Data Committee [74].

3. Results and Analysis

3.1. Raster-Based Analysis from Seasonal Changes

Figure 8 illustrates the results of applying the thresholding technique to four Sentinel-1 SAR images covering two seasons (wet and dry) and tidal states (high and low). Figure 8a,c is derived from Sentinel-1 SAR images acquired during the wet season at 2.10 m and 0.78 m tidal height, respectively. Figure 8b,d is derived from Sentinel-1 SAR images acquired during the dry season at 2.14 m and 0.93 m tidal height, respectively. A visual inspection of the images confirms similarity in shoreline position along the open coast but substantive differences in the complex creek areas.

3.2. Raster-Based Accuracy Assessment from SAR imagery

The results of the raster-based accuracy assessment based on the analysis of each of the twelve images are summarised in Table 2. Taking all statistics into account, the overall accuracy across all raster-based classifications of Sentinel-1 SAR imagery ranges from 95 to 99%. The user's accuracy ranged between 86 and 100% for water bodies, and 93 and 100% for land areas. The producer's accuracy ranged between 95 and 100% for water bodies, and 90 and 100% for land areas. It is worth noting that the variations in the accuracy measures may in part be due to tidal state differences between the baseline data (Google Earth imagery) and the segmented Sentinel-1 images. The kappa coefficient, which is consistently high for each image regardless of season or tidal state, confirms a high level of consistency can be achieved using the threshold-based classification.

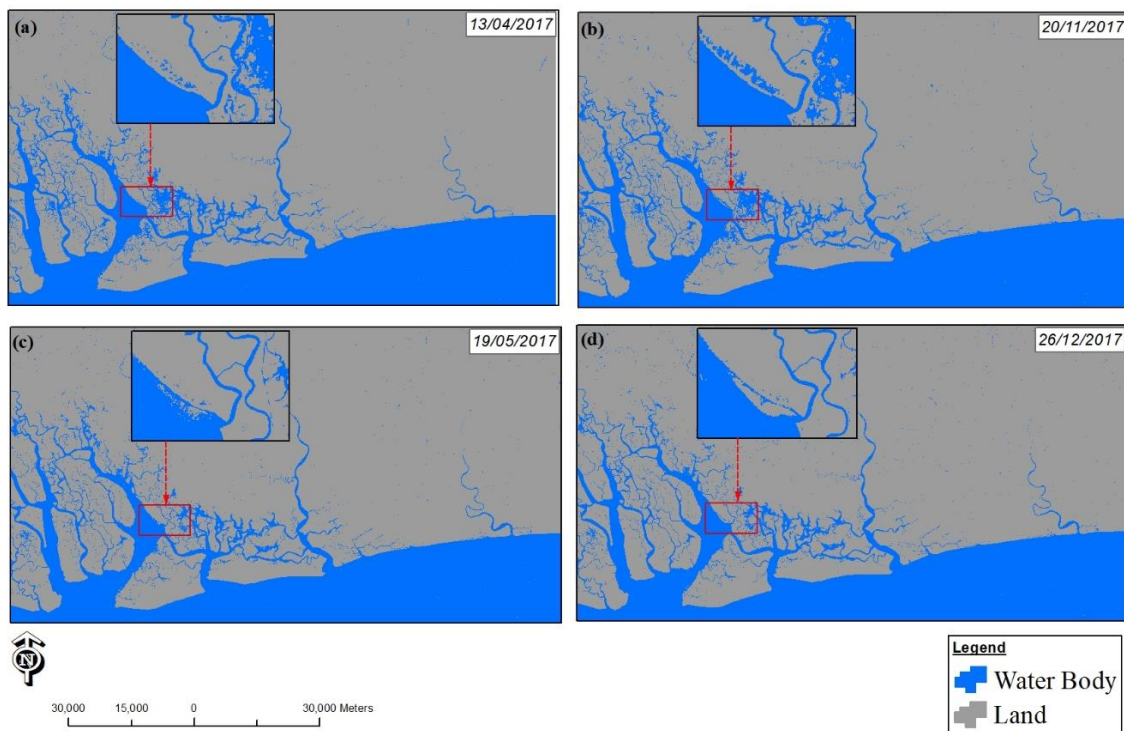


Figure 8. Binary classification of Sentinel-1 images into land and water body classes, showing the images retrieved on (a) 13 April 2017, (b) 20 November 2017, (c) 19 May 2017, and (d) 26 December 2017.

Table 2. Raster-based accuracy assessment for threshold-derived shorelines from Sentinel-1.

Image Acquisition Date	Feature Classes	Accuracy metric				Tide Level	Season
		Producer's Accuracy (%)	User's Accuracy (%)	Overall Accuracy (%)	Kappa Coefficient		
12 January 2017	Water Body	100	89	97	0.93	High	Dry
	Land	90	100				
5 February 2017	Water Body	99	97	98	0.96	Low	Dry
	Land	97	99				
1 March 2017	Water Body	100	93	97	0.93	High	Wet
	Land	93	100				
13 March 2017	Water Body	100	89	95	0.89	High	Wet
	Land	90	100				
13 April 2017	Water Body	100	93	97	0.93	High	Wet
	Land	93	100				
19 May 2017	Water Body	100	96	98	0.96	Low	Wet
	Land	96	100				
17 June 2017	Water Body	100	99	99	0.99	Low	Wet
	Land	99	100				
18 July 2017	Water Body	100	98	99	0.98	Low	Wet
	Land	98	100				

Table 2. Cont.

Image Acquisition Date	Feature Classes	Accuracy metric				Tide Level	Season
		Producer's Accuracy (%)	User's Accuracy (%)	Overall Accuracy (%)	Kappa Coefficient		
16 August 2017	Water Body	99	98	98	0.97	Low	Wet
	Land	99	98				
21 September 2017	Water Body	99	95	97	0.94	High	Wet
	Land	95	99				
20 November 2017	Water Body	95	95	97	0.95	High	Dry
	Land	100	100				
26 December 2017	Water Body	99	99	99	0.98	Low	Dry
	Land	99	99				

3.3. Vector-Based Analysis Using Regions of Interest (ROI)

Figures 9 and 10 show examples of the extent to which the vectorized shorelines derived from the Sentinel-1 SAR imagery compared to the manually digitised Sentinel-2 MSI waterlines for different regions of interest (ROI). In the open coastal environment, there is a decrease in the differences between the SAR-derived shoreline and the reference data decreases from west to east, especially at low tide. Figure 9a illustrates the difference between the shoreline's positions for an area of open coast at the western side of the image, which ranges from 11 to 43 m for the high tide shoreline, and 7 to 34 m for the low tide shoreline (for all these differences, positive values indicate that the SAR line is landward of the reference data line, and negative values indicate the opposite). In an area of open coast in the middle of the image (Figure 9b), the agreement ranges from 4.7 to 7.9 m for the high tide shoreline and -8.9 to 7.0 m for the low tide shoreline. In an area of open coast to the east of the image (Figure 9c), the differences for high tide shoreline and low tide shoreline range from -4.8 and 16.4 m, respectively. This variation seems to largely be a consequence of differences in the image acquisition times.

In the complex creek environment, as illustrated in Figure 10, the overall performance of the method against the reference data seems to be consistent. The region of interest in the complex creek environment was selected based on tidal influence and land cover of the study area. In freshwater-dominant areas, such as those illustrated in Figure 10b, which have little or no tidal influence, the derived shorelines are in close agreement with the reference data for both high mean waterline (HMWL) and low mean waterline (LMWL), with offsets ranging from -1.6 to 11.0 m and -4.0 to 5.8 m for HMWL and LMWL, respectively. In the estuary, which is dominated by mangrove, the derived shorelines show a similar degree of offset from the reference data, with values ranging from 0 to 10.3 m and -3.8 to 17.5 m for HMWL and LMWL, respectively. However, Figure 10d shows that, in the mudflat area, while the two MWL estimates are in good agreement at high water, the SAR method identifies additional land–water boundaries landward of this. Thus, at low water, the two MWL estimates do not overlap; the reference data provide an approximately straight MWL that is seaward of any part of the SAR-derived MWL, while the SAR-derived MWL itself is much more complex in form and spreads across the mudflat area. Together, these give differences from 69.1 to 369.3 m. The present study interprets these differences as being due to relatively subtle variations in surface roughness and homogeneous scattering on the mudflats, which affect the backscatter intensity measured by the SAR instrument.

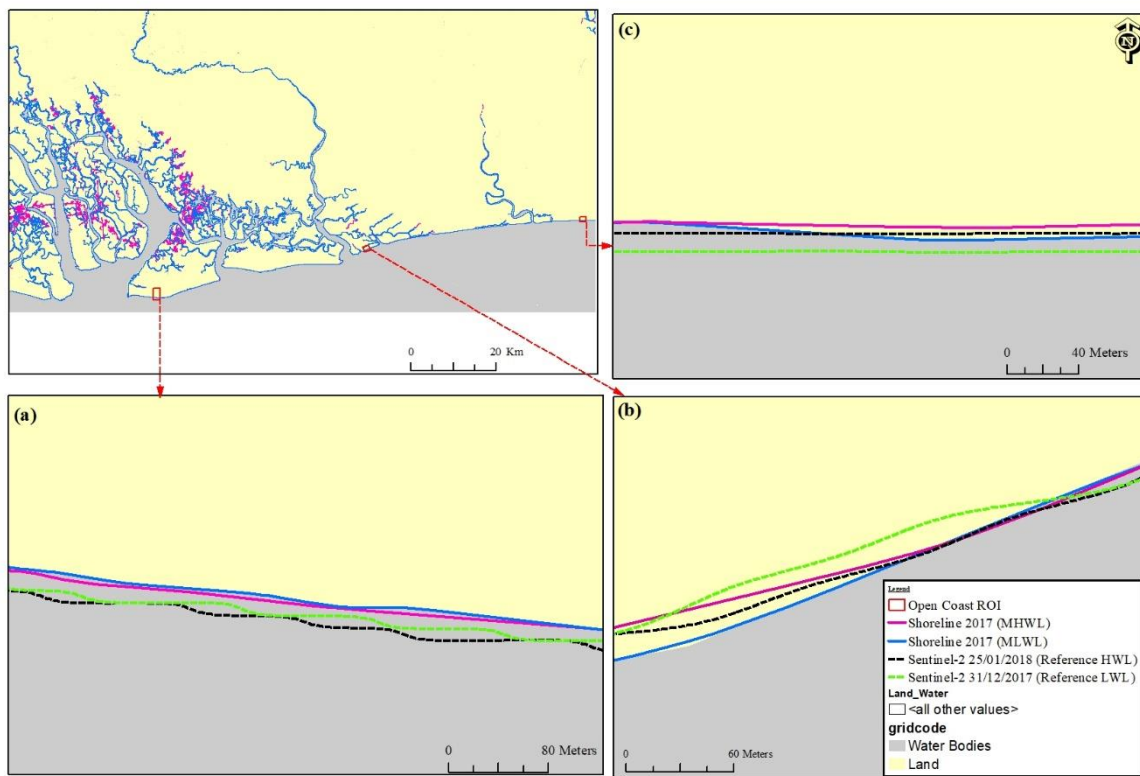


Figure 9. Delineated shorelines overlaid on the reference data, showing the (a–c) details of the delineated shorelines in an open coast.

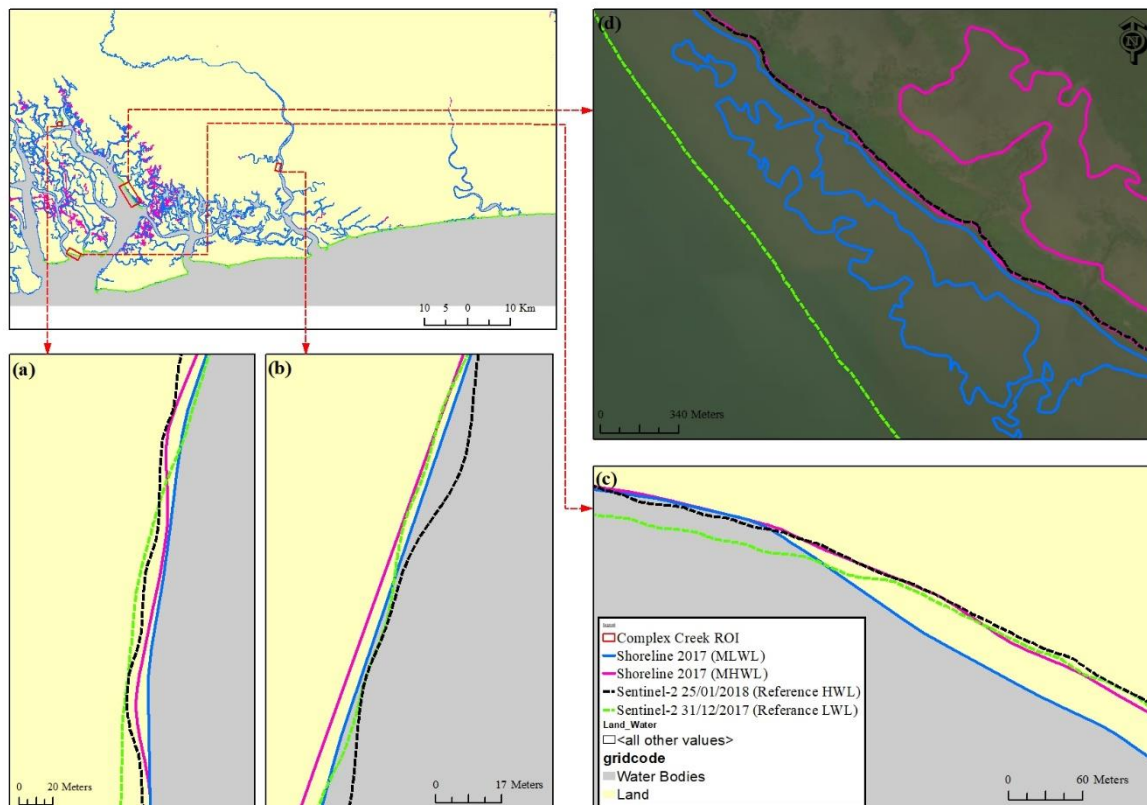


Figure 10. Delineated shorelines overlaid on the reference data. (a–d) Detail of the delineated shorelines in a complex creek environment.

3.4. Positional Accuracy Assessment from Shoreline Positions

Figures 9 and 10 illustrate the level of agreement between the derived shorelines and the reference data for some selected regions of interest. A positional accuracy assessment was conducted using Sentinel-2 MSI as a reference dataset to statistically evaluate the overall accuracy of the low and high tide shorelines derived from the Sentinel-1 SAR data. Table 3 summarises the positional accuracy statistics for shorelines on the open coast and complex creek ROIs. In the open coast ROI, the ranges of the accuracy statistics were from 9.17 m to 34.63 m for the RMSE; from 5.11 m to 13.94 m for the SD; from 14.38 m to 48.36 m for the absolute circular error (ACE) at a 90% confidence level; and from 15.45 m to 41.40 m for the relative circular error (RCE). In the complex creek ROI, the corresponding values ranged from 4.11 m to 213.39 m for the RMSE; from 2.57 m to 120.33 m for the SD; from 6.56 m to 331.01 m for the absolute circular error (ACE) at a 90% confidence level; and from 7.74 m to 396.28 m for the relative circular error (RCE). However, of the seven derived shoreline datasets in both the open coast and complex creek ROI, only five have an RMSE greater than 10 m (one pixel), while the ACE and RCE results of the derived shorelines shows that the value ranges from -2.02 to 10.89 m.

Table 3. Results of the positional accuracy assessment, illustrating the statistics of the differences between shoreline positions derived from Sentinel-1 SAR and Sentinel-2 multispectral optical band imagery.

Location	Zone	Tidal Level	Number of Observation	Mean of Residual	RMSE	SD	ACE	RCE
Figure 8a	Open Coast	MHWL	213	32.36	34.63	12.37	48.36	37.47
Figure 8a	"	MLWL	213	30.85	33.59	13.32	48.07	40.46
Figure 8b	"	MHWL	111	10.22	14.83	10.8	24.20	31.97
Figure 8b	"	MLWL	111	15.71	20.96	13.94	33.80	41.40
Figure 8c	"	MHWL	263	7.41	9.17	5.4	14.38	16.40
Figure 8c	"	MLWL	263	13.30	14.24	5.11	19.90	15.45
Figure 9a	Complex Creek	MHWL	114	7.177	8.72	4.97	13.61	14.86
Figure 9a	"	MLWL	117	10.30	12.10	6.39	18.57	18.39
Figure 9b	"	MHWL	110	4.34	5.1	2.69	7.83	8.17
Figure 9b	"	MLWL	110	3.22	4.11	2.57	6.56	7.74
Figure 9c	"	MHWL	130	6.17	8.51	5.89	13.79	18.01
Figure 9c	"	MLWL	129	22.84	29.69	19.04	47.52	58.92
Figure 9d	"	MHWL	354	10.01	13.17	8.57	21.07	26.14
Figure 9d	"	MLWL	379	176.34	213.39	120.33	331.01	396.28

4. Discussion

This study has explored the capability of using Sentinel-1 imagery to accurately delineate shorelines in the Niger delta region at high-tide and low-tide conditions from dual SAR polarisation (VV and VH) data by (i) segmenting images into two classes (water and land); (ii) defining the boundary between them using histogram-minimum thresholding; (iii) vectorizing and smoothing that boundary using tools built into ArcGIS; and (iv) averaging the shoreline positions over multiple images taken near high and low tides over the course of one year. Using this type of data to delineate waterlines has been previously explored by a number of other researchers [46,47,49,50,52], but exploring the ability of this type of technique to delineate the shoreline at specific tidal states (high and low water in this case), as this study presents here, but does not appear to have been reported in the literature search to date. Liu et al. [51] investigated the construction of tidal flat digital

elevation models (DEMs) using waterlines derived from satellite imagery including SAR data at different tidal states but assumed the accuracy of the waterline delineation methods they adopted. That study [51] investigated the delineation of waterlines at different tidal states in a similar way to that presented here, but the researchers used optical satellite imagery, which would not be possible in our study area (i.e., the Niger Delta coastline) because of the issue of cloud cover, which takes up 8/12 months of the year. In another study, Omari et al. [75] studied the use of polarimetric SAR data to map inter-tidal zones but used aerial photographs from unmanned airborne vehicles (UAVs) to train an image classification process to distinguish wet and dry areas. Here, our intention was to develop method with a cost as low as possible for application in relatively data-deficient countries such as Nigeria; thus, our classification is untrained.

The method presented in this study provides a simple, robust, objective, and cost-effective approach for monitoring shoreline positions in the coastal environment that avoids problems of cloud cover and is therefore particularly appropriate for equatorial contexts such as the Niger delta. The images are free to download from a publicly accessible website; the segmentation process using histogram frequency minima was consistent across all the images used and did not require manual adjustment; and the vectorization of the waterline is achievable via standard tools available in most GIS software packages. Thus, the whole process is amenable to any operator with access to the internet and a GIS. The positional accuracy attained from this method is encouraging, in that it has an RMSE of the order of one pixel (10 m) in most of the area analysed (with notable exceptions, which are discussed further below). The accuracy measures found are dependent on the accuracy of the reference data itself. Due to unavailability of waterline data from the relevant national ministry/agency, such as the reference data used by, for example, Pelich et al. [52], the positional accuracy results presented here relied on manually digitalized waterlines from optical data from the sister satellite (Sentinel-2) of the satellite from which the SAR data were recorded (Sentinel-1). In previous studies, as identified in Section 1, assessing the positional accuracy of derived shorelines has not been straightforward due to factors including sensor type, sensor acquisition geometry, and acquisition times (and thus tidal state) differences [76]. In the present study, the sensor geometry of the two data sources varied: the incidence angle of Sentinel-1 SAR ranges from 29.1° to 46°, while the Sentinel-2 MSI incidence angle is 20.6°. Secondly, as noted above, the difference in data acquisition times may have influenced the accuracy of the results due to coastal geomorphological changes in the time between acquisition of each dataset. However, as these differences would only reduce accuracy measures, the PAAT output values listed in Table 3 are upper limits of the accuracy of the method presented.

There are a number of noteworthy ways in which the proposed method performs well. The derived shorelines are fully continuous, with no breaks. Thus, the creation of averaged imagery from dual-polarisation data, segmentation, vectorization and smoothing processes used to generate them are shown to be appropriate for this task. This finding aligns with those of previous studies, which have found histogram thresholding techniques to be capable of classifying land and water body in a subjective, fast, and repeated way [9,77,78]. This method also has the benefit of being simple to operate and thus appropriate in contexts where operator expertise may be limited. There is a clear difference between the shoreline derived during the wet and dry seasons. In agreement with many others (op. cit.), it also demonstrates the value of combining VV- and VH-polarised data to create dual-polarised images prior to applying the segmentation and delineation processes.

A key limitation of the method is the relatively small number of images available within the space of a year that fall into the category of being recorded at 'high' or 'low' tide. The cut-offs for these categories are arbitrary; however, there is a trade-off in that for, say, high tide, the lower the cut-off, the more images can be used to derive a shoreline position, but those additional images will come from further away from the maximum high tide, thus reducing the average height of the tide. The higher the cut-off, the more strictly 'high' tide the derived shoreline will be, but fewer images will be usable. Without

ground-based information on the across-shore topographic variations at each point on the coast, matching images to their precise point in the tidal cycle will not allow the high tide line to be extrapolated from waterlines for differences in tidal phases; therefore, in data-sparse environments like the Niger delta, an appropriate balance between the number of images used to derive the high tide line and the strictness of the definition of high tide images needs to be struck. However, as more images are recorded over time, it should become possible to develop 3D terrain models (assuming that accurate tidal height data are available), and these can be gradually filled in as the images will inevitably come from different points in the tidal cycle. This would lead to a more reliable high and low tide line delineation but would take several years to accumulate.

The most notable limitation of the method described, as evidenced by the results presented, is its poor performance in delineating the shoreline at low water in areas of inter-tidal mudflats within the estuarine and complex creek ROIs. Figure 8d shows that the LWL derived from the SAR imagery is landward of that observable in the corresponding optical image and appears to be distinguishing between two regions of the inter-tidal zone (i.e., the area between the high and low waterlines in the optical image). The difference between these two regions is not clear but given that SAR reflectance is dependent on surface roughness and dielectric constant, the regions may be distinguished by the type of material that dominates them (e.g., pebbles, sand, mud or possibly biota such as shellfish or seaweed) or by subtle variations in their height, which lead to slightly raised areas drying out more quickly during receding tides. A solution to this problem may require a more sophisticated approach to one or more stages of the process described and requires further study that is beyond the scope of this paper.

Despite the limitations, notably the relatively small number of images available that were recorded at high or low tide, this method provides a simple, objective, and cost-effective approach to the monitoring of shorelines at high and low tide. However, various recent studies suggest potential ways forward in this respect of improving data availability and providing solutions, which include developing vulnerability maps [79]. Other areas for future work that could be applied in this study are machine learning, optimization schemes and deep learning [55,80–83]. For example, Tajima et al. [55] used an artificial neural network (ANN) with SAR imagery data to establish a shoreline detection method considering accuracies from the classification carried out via machine learning. An et al. [80] used a fuzzy C-means approach combined with a wavelet decomposition algorithm to reduce speckle in SAR imagery and thus improve the segmentation process and, consequently, the boundary definition. Wei et al. [81] developed a geometric active contour model to identify shorelines from SAR imagery where the land–water boundary is weakly defined. Other studies include the use of Sentinel-1 SAR imagery for flooding investigation using Hybrid Swarm Optimized Multilayer Neural Network [82] and deep learning [83]. These studies all portray further applications that could be conducted in this area.

The use of Google Earth images in this present study as the reference data is necessary because Google Earth imagery is needed at first to evaluate all the results, more evaluation was carried out in this research to ensure that the Google Earth imagery is not erroneous as qualified reference data since it is a well-validated data source [29,36,84]. Based on the focus of the study, Google Earth imagery was only used to assess the raster-based accuracy of the segment backscattered due to the extent of the study. The confusion matrix was used because it is a simple cross-tabulation of the class labels allocated by the classification of the map data against the reference data (Google Earth). Although, a vital limitation of the approach taken in this study is that while it is suitable to only use the high-resolution Google Earth images from more recent times than 2018, the quality of the imagery output under low-tide conditions obtained when assessing the raster segmentation results will differ as the more recent ones will be better. Additionally, due to the quality demand, some analysed images are acquired under high-tide conditions. However, the reason these image data from Sentinel-2 MSI imagery were used to assess positional accuracy is that the authors want to use uniform satellite imagery for low and high tide from the same Sentinel

family. In this study, we acknowledged the limitations experienced by the data because the tidal height used in the study year has a significant impact on the availability of data. It is worth noting that the most important aspect in characterising the study's data is that the data cut across two seasons (wet and dry). The availability of such data based on the method used might vary from region to region across the globe. The reference data from Google Earth software were only used to assess the raster-based segmentation of land and water bodies in the SAR images. The Google Earth imagery was only used to assess the user's accuracy, the producer's accuracy, the overall accuracy, and the kappa coefficient.

While the method used in the study is the threshold-based water body segmentation approach, it uses data from SAR imagery that are not very recent and somewhat out-of-date (as of 2018) and appear arbitrary; however, these were the available data in the data repository used during the data retrieval, as this study was conducted at different stages. In addition, there are many advanced methods, both conventional and more recently enhanced machine learning (and deep learning) methods, that can achieve a very high accuracy with high stability. However, there are studies that have shown that both machine learning and deep learning methods have strengths and limitations. Some studies have used threshold-based methods with combinations of other methods, as in the most recent study [54]. In short, it has also been evidently presented that there are several methods that could be considered for segmenting SAR imagery, such as machine learning and deep learning [82,83,85,86], developing openly available digital shoreline analysis systems like ODSAS [87], or having an SAR-imagery data repository like the Copernicus Open Access Hub (previously referred to as Sentinels Scientific Data Hub) [39,40,88]. However, there is no generally accepted method of segmenting imagery currently, especially when segmenting shorelines.

Overall, the method presented in the present study has further limitations as it lacks the sophistication of some other methods reported in the literature but emphasizes utility in data-sparse contexts and provides delineations of high and low shorelines that this study argues are sufficiently continuous and reliable, especially on open coasts, for practical applications such as coastal vulnerability and flood risk assessments. This argument is supported by the comparisons with optical imagery presented. Although there are problems in certain contexts with the low tide shoreline, for applications such as these, it is the high tide line that is of concern, and the method works well in all ROIs in that respect. Based on the metric used, we suggest other precision-based approaches as opposed to only accuracy, such as the use of intersection over union. For the positional accuracy assessment tool (PAAT), the point-based standard methodology (PBSM) provides a more robust metric for assessing shoreline position. The PAAT tool has been found to be a useful support raster-vector analysis on ArcGIS software. This is because it computes the random and systematic errors between a reference dataset and a target dataset, expressing differences through three metrics: mean residual, root mean square error (RMSE), and standard deviation (SD).

5. Conclusions

Given that satellite image analysis has been identified to be a potentially powerful tool for monitoring shoreline positions, we utilised it in this research to solve a coastal problem of shoreline delineation. The present study explores the use of multi-temporal, dual-polarised Sentinel-1 synthetic aperture radar (SAR) imagery with a spatial resolution of 10 m for delineating shorelines in a complex environment with a cloud-heavy climate. The case study for the investigation is in the Niger delta region of Nigeria, which is a developing country in Africa. This study focused on exploring and testing the capability of using multitemporal waterlines from SAR images to derive shoreline positions at high and low tidal states. From 54 Sentinel-1 images recorded in 2017, the study selected 12 images to represent both high and low tidal states. These were spread across the wet and dry seasons in order to account for seasonal differences. Shoreline positions were obtained by identifying the land–water boundary via segmentation using histogram-minimum

thresholding, vectorizing and smoothing that boundary, and averaging its position over multiple waterlines. This study makes a significant contribution to shoreline delineation in coastal regions, and the model applied in this study adds to the understanding of SAR. The approach considered in this research also highlights the novelty in data collection and processing for SAR.

From this study, it was observed that the land–water segmentation had an overall accuracy of 95–99%. Accuracy was assessed against reference waterlines derived manually from Sentinel-2 multispectral instrument optical imagery. It showed differences between wet and dry season shoreline positions in areas dominated by complex creek networks, but similarities along open coasts. The SAR-derived shorelines deviated from the reference lines by a maximum of 43 m (approximately four pixels), and often less than 10 m (one pixel) in most locations (open coast, estuarine, complex creek networks) at high and low tide. The notable exception was the low tide line in areas with extensive inter-tidal flats. In those cases, the processing method picked up apparently subtle variations, which led to it identifying shorelines 70 to 370 m from the reference lines. However, for applications such as coastal vulnerability assessment, the high tide shoreline is of greater importance; thus, depending on the application of interest, problems with low tide shoreline delineation may be irrelevant. Overall, despite the limitations, notably the relatively small number of images available that were recorded at high or low tide, this method provides a simple, objective, and cost-effective approach to monitoring shorelines at high and low tide.

The study achieves the stated aims of developing a robust and repeatable segmentation technique to delineate shorelines at high and low tide; to assess the accuracy of the derived shorelines against reference data; and to infer the implications of our findings for the application of this approach to aspects of coastal management. In so doing, this study has presented a simple method that overcomes the problem of extensive cloud cover and provides a viable approach to shoreline delineation in data-sparse contexts where operator expertise in image analysis techniques may be limited. To develop this method further, the issue of poor low tide line delineation in some conditions needs to be addressed, and the possibility of building up terrain models from the ever-growing archive of high-resolution imagery should be explored. By carrying this out, SAR imagery could be complemented by optical imagery recorded on occasions when cloud cover is low, allowing ongoing referencing and accuracy assessment of the SAR-derived shorelines to be carried out. Future works should consider assessing the shoreline delineation accuracies in different regions (open coast, complex creek networks, etc.). Additionally, future directions could be considered in using other methods of imagery to obtain geographical and environmental data in the Niger Delta area of Nigeria. Lastly, it should be noted that more metrics should be used to provide a more comprehensive evaluation, such as precision, and intersection over union, instead of only using accuracy in future studies.

Author Contributions: Conceptualization, E.C.D.; methodology, E.C.D. and C.V.A.; software, E.C.D., A.K.O. and C.V.A.; validation, E.C.D., A.K.O. and C.V.A.; formal analysis, E.C.D., A.K.O. and C.V.A.; investigation, E.C.D.; resources, E.C.D., A.K.O. and C.V.A.; data curation, E.C.D., A.K.O. and C.V.A.; writing—original draft preparation, E.C.D.; writing—review and editing, E.C.D., A.K.O. and C.V.A.; visualization, E.C.D., A.K.O. and C.V.A.; supervision, E.C.D.; project administration, E.C.D., A.K.O. and C.V.A.; funding acquisition, E.C.D., A.K.O. and C.V.A. All authors have read and agreed to the published version of the manuscript.

Funding: This research also acknowledges the funding support of Lancaster University: Engineering Department Studentship Award; Niger Delta Development Commission (NG): NDDC Overseas Postgraduate Scholarship; Standards Organisation of Nigeria (NG): SON Study; Engineering and Physical Sciences Research Council (UK): EPSRC's Doctoral Training Centre (DTC); Tertiary Education Trust Fund (NG): TETFUND. Universiti Tenaga Nasional (UNITEN), Malaysia: BOLD25 Initiative is also acknowledged. There was no financial support received from any organization except for the doctoral research conducted with which this study was done, but highly appreciated.

Institutional Review Board Statement: Not applicable.

Informed Consent Statement: Not applicable.

Data Availability Statement: The data supporting the reported results are not shared because they are used for more studies. It may be available upon reasonable request to the corresponding authors. However, the Multi-temporal Sentinel-1 Level 1 SAR C-band Ground Range Detected (GRD) data can be acquired from the European Space Agency (ESA) Copernicus Open Access Hub, as freely and openly available online at: <https://scihub.copernicus.eu/> (accessed on 23 July 2023). See Ref. [88].

Acknowledgments: The principal author acknowledges the support of Lancaster Environmental Centre (LEC) at Lancaster University in carrying out part of this work in a doctoral research. The authors also acknowledge the software developers for the packages used on this study, like ArcGIS and Google Earth. We also appreciate the Copernicus programme and European Space Agency (ESA) for the use of the SAR imagery data. The authors also appreciate the feedback from the reviewers to improve the quality of this paper.

Conflicts of Interest: There is no conflict of interest from the authors.

References

1. Porzycka-Strzelczyk, S.; Strzelczyk, J.; Szostek, K.; Dwornik, M.; Leśniak, A.; Bała, J.; Franczyk, A. Information Extraction from Satellite-Based Polarimetric SAR Data Using Simulated Annealing and SIRT Methods and GPU Processing. *Energies* **2022**, *15*, 72. [CrossRef]
2. Oloyede, M.O.; Williams, A.B.; Ode, G.O.; Benson, N.U. Coastal Vulnerability Assessment: A Case Study of the Nigerian Coastline. *Sustainability* **2022**, *14*, 2097. [CrossRef]
3. Liu, H.; Zhou, B.; Bai, Z.; Zhao, W.; Zhu, M.; Zheng, K.; Yang, S.; Li, G. Applicability Assessment of Multi-Source DEM-Assisted Separately InSAR Deformation Monitoring Considering Two Topographical Features. *Land* **2023**, *12*, 1284. [CrossRef]
4. Herrera-Franco, G.; Montalván, F.J.; Velastegui-Montoya, A.; Caicedo-Potosí, J. Vulnerability in a Populated Coastal Zone and Its Influence by Oil Wells in Santa Elena, Ecuador. *Resources* **2022**, *11*, 70. [CrossRef]
5. Bukvic, A.; Rohat, G.; Apotsos, A.; de Sherbinin, A. A Systematic Review of Coastal Vulnerability Mapping. *Sustainability* **2020**, *12*, 2822. [CrossRef]
6. Anfuso, G.; Postacchini, M.; Di Luccio, D.; Benassai, G. Coastal Sensitivity/Vulnerability Characterization and Adaptation Strategies: A Review. *J. Mar. Sci. Eng.* **2021**, *9*, 72. [CrossRef]
7. Gonçalves, V.; Albuquerque, A.; Almeida, P.G.; Cavaleiro, V. DRASTIC Index GIS-Based Vulnerability Map for the Entre-os-Rios Thermal Aquifer. *Water* **2022**, *14*, 2448. [CrossRef]
8. Hamid, A.; Din, A.; Abdullah, N.; Yusof, N.; Hamid, M.; Shah, A. Exploring space geodetic technology for physical coastal vulnerability index and management strategies: A review. *Ocean Coast. Manag.* **2021**, *214*, 105916. [CrossRef]
9. Niedermeier, A.; Romaneessen, E.; Lehner, S. Detection of coastlines in SAR images using wavelet methods. *IEEE Trans. Geosci. Remote Sens.* **2000**, *38*, 2270–2281. [CrossRef]
10. Komar, P.D. *Beach Processes and Sedimentation*; Prentice Hall: Hoboken, NJ, USA, 1998.
11. Bouchahma, M.; Yan, W. Monitoring shoreline change on Djerba Island using GIS and multi-temporal satellite data. *Arab. J. Geosci.* **2013**, *7*, 3705–3713. [CrossRef]
12. Ferreira, O.; Garcia, T.; Matias, A.; Taborda, R.; Alveirinho Dias, J. An integrated method for the determination of set-back lines for coastal erosion hazards on sandy shores. *Cont. Shelf Res.* **2006**, *26*, 1030–1044. [CrossRef]
13. Allan, J.C.; Komar, P.D.; Priest, G.R. Shoreline Variability on the High-Energy Oregon Coast and its Usefulness in Erosion Hazard Assessments. *J. Coast. Res.* **2003**, *38*, 83–105.
14. Langat, P.K.; Kumar, L.; Koech, R. Monitoring river channel dynamics using remote sensing and GIS techniques. *Geomorphology* **2019**, *325*, 92–102. [CrossRef]
15. Boak, E.H.; Turner, I.L. Shoreline Definition and Detection: A Review. *J. Coast. Res.* **2005**, *214*, 688–703. [CrossRef]
16. Zollini, S.; Alicandro, M.; Cuevas-González, M.; Baiocchi, V.; Dominici, D.; Buscema, P.M. Shoreline Extraction Based on an Active Connection Matrix (ACM) Image Enhancement Strategy. *J. Mar. Sci. Eng.* **2019**, *8*, 9. [CrossRef]
17. Paz-Delgado, M.V.; Payo, A.; Gómez-Pazo, A.; Beck, A.-L.; Savastano, S. Shoreline Change from Optical and Sar Satellite Imagery at Macro-Tidal Estuarine, Cluffed Open-Coast and Gravel Pocket-Beach Environments. *J. Mar. Sci. Eng.* **2022**, *10*, 561. [CrossRef]
18. Pajak, M.J.; Leatherman, S. The high water line as shoreline indicator. *J. Coast. Res.* **2002**, *18*, 329–337.
19. Zheng, H.; Li, X.; Wan, J.; Xu, M.; Liu, S.; Yasir, M. Automatic Coastline Extraction Based on the Improved Instantaneous Waterline Extraction Method and Correction Criteria Using SAR Imagery. *Sustainability* **2023**, *15*, 7199. [CrossRef]
20. Fu, W.; Ma, J.; Chen, P.; Chen, F. Remote Sensing Satellites for Digital Earth. In *Manual of Digital Earth*; Guo, H., Goodchild, M.F., Annoni, A., Eds.; Springer: Singapore, 2020; pp. 55–123. [CrossRef]
21. Niedermeier, A.; Hoja, D.; Lehner, S. Topography and morphodynamics in the German Bight using SAR and optical remote sensing data. *Ocean Dyn.* **2005**, *55*, 100–109. [CrossRef]
22. Ochege, F.U.; George, R.T.; Dike, E.C.; Okpala-Okaka, C. Geospatial assessment of vegetation status in Sagbama oilfield environment in the Niger Delta region, Nigeria. *Egypt. J. Remote Sens. Space Sci.* **2017**, *20*, 211–221. [CrossRef]

23. McFeeters, S.K. The use of the Normalized Difference Water Index (NDWI) in the delineation of open water features. *Int. J. Remote Sens.* **2007**, *17*, 1425–1432. [[CrossRef](#)]
24. Fisher, A.; Flood, N.; Danaher, T. Comparing Landsat water index methods for automated water classification in eastern Australia. *Remote Sens. Environ.* **2016**, *175*, 167–182. [[CrossRef](#)]
25. Xu, H. Modification of normalised difference water index (NDWI) to enhance open water features in remotely sensed imagery. *Int. J. Remote Sens.* **2007**, *27*, 3025–3033. [[CrossRef](#)]
26. Crist, E.P. A TM Tasseled Cap equivalent transformation for reflectance factor data. *Remote Sens. Environ.* **1985**, *17*, 301–306. [[CrossRef](#)]
27. Kelly, J.T.; Gontz, A.M. Using GPS-surveyed intertidal zones to determine the validity of shorelines automatically mapped by Landsat water indices. *Int. J. Appl. Earth Obs. Geoinf.* **2018**, *65*, 92–104. [[CrossRef](#)]
28. Feyisa, G.L.; Meilby, H.; Fensholt, R.; Proud, S.R. Automated Water Extraction Index: A new technique for surface water mapping using Landsat imagery. *Remote Sens. Environ.* **2014**, *140*, 23–35. [[CrossRef](#)]
29. Vos, K.; Splinter, K.D.; Harley, M.D.; Simmons, J.A.; Turner, I.L. CoastSat: A Google Earth Engine-enabled Python toolkit to extract shorelines from publicly available satellite imagery. *Environ. Model. Softw.* **2019**, *122*, 104528. [[CrossRef](#)]
30. Toure, S.; Diop, O.; Kpalma, K.; Maiga, A.S. Shoreline Detection using Optical Remote Sensing: A Review. *ISPRS Int. J. Geo-Inf.* **2019**, *8*, 75. [[CrossRef](#)]
31. Lee, J.; Jurkevich, I. Coastline Detection And Tracing In SAR Images. *IEEE Trans. Geosci. Remote Sens.* **1990**, *28*, 662–668.
32. Mason, D.; Davenport, I. Accurate and efficient determination of the shoreline in ERS-1 SAR images. *IEEE Trans. Geosci. Remote Sens.* **1996**, *34*, 1243–1253. [[CrossRef](#)]
33. Spinosa, A.; Ziemba, A.; Saponieri, A.; Navarro-Sanchez, V.D.; Damiani, L.; Serafy, G.E. Automatic Extraction of Shoreline from Satellite Images a new approach. In Proceedings of the 2018 IEEE International Workshop on Metrology for the Sea; Learning to Measure Sea Health Parameters (MetroSea), Bari, Italy, 8–10 October 2018; pp. 33–38. [[CrossRef](#)]
34. Wang, D.; Liu, X. Coastline Extraction from SAR Images Using Robust Ridge Tracing. *Mar. Geodesy* **2019**, *42*, 286–315. [[CrossRef](#)]
35. Chaturvedi, S.K.; Banerjee, S.; Lele, S. An assessment of oil spill detection using Sentinel 1 SAR-C images. *J. Ocean Eng. Sci.* **2020**, *5*, 116–135. [[CrossRef](#)]
36. Tian, P.; Liu, Y.; Li, J.; Pu, R.; Cao, L.; Zhang, H.; Ai, S.; Yang, Y. Mapping Coastal Aquaculture Ponds of China Using Sentinel SAR Images in 2020 and Google Earth Engine. *Remote Sens.* **2022**, *14*, 5372. [[CrossRef](#)]
37. Obida, C.B.; Blackburn, G.A.; Whyatt, J.D.; Semple, K.T. River network delineation from Sentinel-1 SAR data. *Int. J. Appl. Earth Obs. Geoinf.* **2019**, *83*, 101910. [[CrossRef](#)]
38. Zhang, Y.; Wang, C.; Chen, J.; Wang, F. Shape-Constrained Method of Remote Sensing Monitoring of Marine Raft Aquaculture Areas on Multitemporal Synthetic Sentinel-1 Imagery. *Remote Sens.* **2022**, *14*, 1249. [[CrossRef](#)]
39. ESA. Sentinel-1 SAR User Guide. Sentinel Online—The European Space Agency (ESA), Copernicus Programme. 2023. Available online: <https://sentinel.esa.int/web/sentinel/user-guides/sentinel-1-sar> (accessed on 23 July 2023).
40. Small, D.; Schubert, A. *Guide to Sentinel-1 Geocoding*; Tech. Rep. UZH-S1-GC-AD. Issue: 1.12, Last Updated Date: 19 May 2022; Remote Sensing Lab. Univ. Zurich (RSL): Zürich, Switzerland, 2022; pp. 1–42. Available online: <https://sentinels.copernicus.eu/documents/247904/1653442/Guide-to-Sentinel-1-Geocoding.pdf> (accessed on 23 July 2023).
41. Li, X.-M.; Lehner, S. Algorithm for Sea Surface Wind Retrieval from TerraSAR-X and TanDEM-X Data. *IEEE Trans. Geosci. Remote Sens.* **2014**, *52*, 2928–2939. [[CrossRef](#)]
42. Mouche, A.; Chapron, B. Global C-Band Envisat, RADARSAT-2 and Sentinel-1 SAR measurements in copolarization and cross-polarization. *J. Geophys. Res. Ocean.* **2015**, *120*, 7195–7207. [[CrossRef](#)]
43. Mouche, A.A.; Hauser, D.; Kudryavtsev, V. Radar scattering of the ocean surface and sea-roughness properties: A combined analysis from dual-polarizations airborne radar observations and models in C band. *J. Geophys. Res. Atmos.* **2006**, *111*, 1–18. [[CrossRef](#)]
44. Altese, E.; Bolognani, O.; Mancini, M.; Troch, P.A. Retrieving Soil Moisture Over Bare Soil from ERS 1 Synthetic Aperture Radar Data: Sensitivity Analysis Based on a Theoretical Surface Scattering Model and Field Data. *Water Resour. Res.* **1996**, *32*, 653–661. [[CrossRef](#)]
45. Van Der Wal, D.; Herman, P.M.J.; Wielemaker-Van Den Dool, A. Characterisation of surface roughness and sediment texture of intertidal flats using ERS SAR imagery. *Remote Sens. Environ.* **2005**, *98*, 96–109. [[CrossRef](#)]
46. Bioresita, F.; Hayati, N. Coastline changes detection using Sentinel-1 satellite imagery in Surabaya, East Java, Indonesia. *Geoid* **2016**, *11*, 190. [[CrossRef](#)]
47. Ao, W.; Xu, F.; Li, Y.; Wang, H. Detection and Discrimination of Ship Targets in Complex Background From Spaceborne ALOS-2 SAR Images. *IEEE J. Sel. Top. Appl. Earth Obs. Remote Sens.* **2018**, *11*, 536–550. [[CrossRef](#)]
48. Nunziata, F.; Migliaccio, M.; Li, X.; Ding, X. Coastline Extraction Using Dual-Polarimetric COSMO-SkyMed PingPong Mode SAR Data. *IEEE Geosci. Remote Sens. Lett.* **2014**, *11*, 104–108. [[CrossRef](#)]
49. Ding, X.; Nunziata, F.; Li, X.; Migliaccio, M. Performance Analysis and Validation of Waterline Extraction Approaches Using Single- and Dual-Polarimetric SAR Data. *IEEE J. Sel. Top. Appl. Earth Obs. Remote Sens.* **2015**, *8*, 1. [[CrossRef](#)]
50. Demir, N.; Kaynarca, M.; Oy, S. Extraction of Coastlines with Fuzzy Approach Using Sentinel-1 Sar Image. *Int. Arch. Photogramm. Remote Sens. Spatial Inf. Sci.* **2016**, *XLI-B7*, 747–751. [[CrossRef](#)]

51. Liu, X.; Gao, Z.; Ning, J.; Yu, X.; Zhang, Y. An Improved Method for Mapping Tidal Flats Based on Remote Sensing Waterlines: A Case Study in the Bohai Rim, China. *IEEE J. Sel. Top. Appl. Earth Obs. Remote Sens.* **2016**, *9*, 5123–5129. [[CrossRef](#)]
52. Pelich, R.; Chini, M.; Hostache, R.; Matgen, P.; Lopez-Martinez, C. Coastline Detection Based on Sentinel-1 Time Series for Ship- and Flood-Monitoring Applications. *IEEE Geosci. Remote Sens. Lett.* **2020**, *18*, 1771–1775. [[CrossRef](#)]
53. Dike, E.; Ilic, S.; Whyatt, D.; Folkard, A. Shoreline Delineation in Complex Intertidal Environments Using Sentinel-1 SAR Imagery. GIS Research Conference, UK, 2020, pp. 1–5. Available online: https://eprints.lancs.ac.uk/id/eprint/172143/1/GISRUK_Dike_2020.pdf (accessed on 20 March 2023).
54. Dike, E. Deriving Shorelines from SAR Images to Assess Coastal Vulnerability in Data Poor Regions. Ph.D. Thesis, Lancaster University, Lancaster Environment Centre (LEC), Lancaster, UK, 2022. [[CrossRef](#)]
55. Tajima, Y.; Wu, L.; Watanabe, K. Development of a Shoreline Detection Method Using an Artificial Neural Network Based on Satellite SAR Imagery. *Remote Sens.* **2021**, *13*, 2254. [[CrossRef](#)]
56. IPCC. Climate Change 2007: The Physical Science Basis. In *Contribution of Working Group I to the Fourth Assessment Report of the Intergovernmental Panel on Climate Change*; Solomon, S., Qin, D., Manning, M., Chen, Z., Marquis, M., Averyt, K.B., Tignor, M., Miller, H.L., Eds.; Cambridge University Press: Cambridge, UK; New York, NY, USA, 2007.
57. FMEN. *National Environmental, Economic and Development Study (NEEDS) for Climate Change in Nigeria*; UNFCCC, Ed.; Federal Ministry of Environment: Abuja, Nigeria, 2010. Available online: <https://unfccc.int/files/adaptation/application/pdf/nigerianneeds.pdf> (accessed on 25 July 2023).
58. Agbakwuru, J. Pipeline Potential Leak Detection Technologies: Assessment and Perspective in the Nigeria Niger Delta Region. *J. Environ. Prot.* **2011**, *2*, 1055–1061. [[CrossRef](#)]
59. Agomuoh, A.E.; Ossia, C.V.; Chukwuma, F.O. Asset Integrity Management in Mitigating Oil and Gas Pipeline Vandalism in the Niger Delta Region—Deep Burial Solution. *World J. Eng. Technol.* **2021**, *9*, 565–578. [[CrossRef](#)]
60. Amaechi, C.V.; Reda, A.; Kgosiemang, I.M.; Ja’e, I.A.; Oyetunji, A.K.; Olukolajo, M.A.; Igwe, I.B. Guidelines on Asset Management of Offshore Facilities for Monitoring, Sustainable Maintenance, and Safety Practices. *Sensors* **2022**, *22*, 7270. [[CrossRef](#)] [[PubMed](#)]
61. Ayanlade, A.; Howard, M.T. Environmental impacts of oil production in the Niger Delta: Remote sensing and social survey examination. *Afr. Geogr. Rev.* **2016**, *35*, 272–293. [[CrossRef](#)]
62. Aa, I.; Op, A.; Ujj, I.; Mt, B. A critical review of oil spills in the Niger Delta aquatic environment: Causes, impacts, and bioremediation assessment. *Environ. Monit. Assess.* **2022**, *194*, 816. [[CrossRef](#)] [[PubMed](#)]
63. Obida, C.B.; Blackburn, G.A.; Whyatt, J.D.; Semple, K.T. Counting the cost of the Niger Delta’s largest oil spills: Satellite remote sensing reveals extensive environmental damage with > 1 million people in the impact zone. *Sci. Total. Environ.* **2021**, *775*, 145854. [[CrossRef](#)]
64. Abam, T.K.S. Engineering Geology of the Niger Delta. *J. Earth Sci. Geotech. Eng.* **2016**, *6*, 65–89. Available online: http://www.sciencpress.com/Upload/GEO/Vol%206_3_4.pdf (accessed on 23 July 2023).
65. Danladi, I.B.; Kore, B.M.; Gül, M. Vulnerability of the Nigerian coast: An insight into sea level rise owing to climate change and anthropogenic activities. *J. Afr. Earth Sci.* **2017**, *134*, 493–503. [[CrossRef](#)]
66. Oyegun, C.U.; Lawal, O.; Ogoro, M. Vulnerability of Coastal Communities in Niger Delta Region to Sea Level Rise. *J. Res. Environ. Earth Sci.* **2016**, *2*, 1–8. Available online: <https://www.researchgate.net/profile/Olanrewaju-Lawal-2/publication/303079766> (accessed on 23 July 2023).
67. IPCC. *Climate Change 2013—The Physical Science Basis. Contribution of Working Groups I, II and III to the Fifth Assessment Report of the Intergovernmental Panel on Climate Change*; Sydowed, I., Ed.; Intergovernmental Panel on Climate Change: Geneva, Switzerland; Cambridge University Press: Cambridge, UK, 2013.
68. Usoro, E. Nigeria. In *Encyclopedia of the World’s Coastal Landforms*; Bird, E.C.F., Ed.; Springer: Dordrecht, The Netherlands, 2010.
69. Xie, H.; Luo, X.; Xu, X.; Pan, H.; Tong, X. Automated Subpixel Surface Water Mapping from Heterogeneous Urban Environments Using Landsat 8 OLI Imagery. *Remote Sens.* **2016**, *8*, 584. [[CrossRef](#)]
70. Maglione, P.; Parente, C.; Vallario, A. Coastline extraction using high resolution WorldView-2 satellite imagery. *Eur. J. Remote Sens.* **2017**, *47*, 685–699. [[CrossRef](#)]
71. Sreeekesh, S.; Kaur, N.; Naik, S.R.S. An OBIA and Rule Algorithm for Coastline Extraction from High- and Medium-Resolution Multispectral Remote Sensing Images. *Remote Sens. Earth Syst. Sci.* **2020**, *3*, 24–34. [[CrossRef](#)]
72. Ruiz-Lendínez, J.J.; Ariza-López, F.J.; Ureña-Cámara, M.A. Study of NSSDA Variability by Means of Automatic Positional Accuracy Assessment Methods. *ISPRS Int. J. Geo-Inf.* **2019**, *8*, 552. [[CrossRef](#)]
73. ESRI. *Reviewing the Positional Accuracy Assessment (PAAT) Session Results*; ArcGIS Desktop Help. Environmental Systems Research Institute, Inc. (ESRI), 2012. Available online: <https://webhelp.esri.com/arcgisdesktop/9.3/body.cfm?tocVisible=1&ID=5004&TopicName=Reviewing%20the%20PAAT%20session%20results> (accessed on 20 June 2022).
74. FGDC. Geospatial Positioning Accuracy Standards. In *Part 3: National Standard for Spatial Data Accuracy*; Federal Geographic Data Committee: Reston, VA, USA, 1998.
75. Omari, K.; Chenier, R.; Touzi, R.; Sagram, M. Investigation of C-Band SAR Polarimetry for Mapping a High-Tidal Coastal Environment in Northern Canada. *Remote Sens.* **2020**, *12*, 1941. [[CrossRef](#)]
76. Bruno, M.F.; Molfetta, M.G.; Pratola, L.; Mossa, M.; Nutricato, R.; Morea, A.; Nitti, D.O.; Chiaradia, M.T. A Combined Approach of Field Data and Earth Observation for Coastal Risk Assessment. *Sensors* **2019**, *19*, 1399. [[CrossRef](#)] [[PubMed](#)]

77. Liu, H.; Jezek, K.C. Automated extraction of coastline from satellite imagery by integrating Canny edge detection and locally adaptive thresholding methods. *Int. J. Remote Sens.* **2004**, *25*, 937–958. [[CrossRef](#)]
78. Dellepiane, S.; De Laurentiis, R.; Giordano, F. Coastline extraction from SAR images and a method for the evaluation of the coastline precision. *Pattern Recognit. Lett.* **2004**, *25*, 1461–1470. [[CrossRef](#)]
79. Fotsi, Y.F.; Pouvreau, N.; Brenon, I.; Onguene, R.; Etame, J. Temporal (1948–2012) and Dynamic Evolution of the Wouri Estuary Coastline within the Gulf of Guinea. *J. Mar. Sci. Eng.* **2019**, *7*, 343. [[CrossRef](#)]
80. An, M.; Sun, Q.; Hu, J.; Tang, Y.; Zhu, Z. Coastline Detection with Gaofen-3 SAR Images Using an Improved FCM Method. *Sensors* **2018**, *18*, 1898. [[CrossRef](#)] [[PubMed](#)]
81. Wei, X.; Zheng, W.; Xi, C.; Shang, S. Shoreline Extraction in SAR Image Based on Advanced Geometric Active Contour Model. *Remote Sens.* **2021**, *13*, 642. [[CrossRef](#)]
82. Ngo, P.-T.T.; Hoang, N.-D.; Pradhan, B.; Nguyen, Q.K.; Tran, X.T.; Nguyen, Q.M.; Nguyen, V.N.; Samui, P.; Bui, D.T. A Novel Hybrid Swarm Optimized Multilayer Neural Network for Spatial Prediction of Flash Floods in Tropical Areas Using Sentinel-1 SAR Imagery and Geospatial Data. *Sensors* **2018**, *18*, 3704. [[CrossRef](#)]
83. Bonafilia, D.; Tellman, B.; Anderson, T.; Issenberg, E. Sen1Floods11: A georeferenced dataset to train and test deep learning flood algorithms for Sentinel-1. In Proceedings of the IEEE Computer Society Conference on Computer Vision and Pattern Recognition, Seattle, WA, USA, 14–19 June 2020; pp. 835–845. [[CrossRef](#)]
84. Bentivoglio, R.; Isufi, E.; Jonkman, S.N.; Taormina, R. Deep learning methods for flood mapping: A review of existing applications and future research directions. *Hydrol. Earth Syst. Sci.* **2022**, *26*, 4345–4378. [[CrossRef](#)]
85. Olusola, A.O.; Adedeji, O.; Akpoterai, L.; Ogunjo, S.T.; Olusegun, C.F.; Adelabu, S. Flood Assessment Along Lower Niger River Using Google Earth Engine. In *Soil-Water, Agriculture, and Climate Change*; Dubey, S.K., Jha, P.K., Gupta, P.K., Nanda, A., Gupta, V., Eds.; Springer: Cham, Switzerland, 2022; pp. 329–343. [[CrossRef](#)]
86. Bui, Q.-T.; Nguyen, Q.-H.; Nguyen, X.L.; Pham, V.D.; Nguyen, H.D.; Pham, V.-M. Verification of novel integrations of swarm intelligence algorithms into deep learning neural network for flood susceptibility mapping. *J. Hydrol.* **2020**, *581*, 124379. [[CrossRef](#)]
87. Gómez-Pazo, A.; Payo, A.; Paz-Delgado, M.V.; Delgadillo-Calzadilla, M.A. Open Digital Shoreline Analysis System: ODSAS v1.0. *J. Mar. Sci. Eng.* **2021**, *10*, 26. [[CrossRef](#)]
88. Copernicus. Copernicus Open Access Hub (Previously Known as Sentinels Scientific Data Hub). European Space Agency. 2023. Available online: <https://scihub.copernicus.eu/> (accessed on 23 July 2023).

Disclaimer/Publisher’s Note: The statements, opinions and data contained in all publications are solely those of the individual author(s) and contributor(s) and not of MDPI and/or the editor(s). MDPI and/or the editor(s) disclaim responsibility for any injury to people or property resulting from any ideas, methods, instructions or products referred to in the content.